

# EXPERIMENTAL VALIDATION OF THE KINEMATIC DESIGN OF 3PRS COMPLIANT PARALLEL MECHANISMS

A. Ruiz\*, F. J. Campa\*, C. Roldán-Paraponiaris\*, O. Altuzarra\* and C. Pinto\*

\*Department of Mechanical Engineering, University of the Basque Country UPV/EHU, Escuela Superior de Ingeniería de Bilbao, Alameda Urquijo s/n, 48013, Bilbao, Spain

Corresponding author information:

Francisco J. Campa

Phone: +34 946014006

Fax: +34 946014215

Email: fran.campa@ehu.eus

## ABSTRACT

In this paper, a procedure for the kinematic design of a 3-PRS compliant parallel manipulator of 3 degrees of freedom is proposed. First, under the assumption of small displacements, the solid body kinematics of the 3-PRS has been studied, performing a comprehensive analysis of the inverse and forward kinematic problem, and calculating the rotations that the revolute and spherical flexure joints must perform. Then, after defining some design requirements and therefore the necessary displacements to fulfill, a design process based on the finite element calculations has been established, giving the necessary guidelines to reach the optimal solution on a 3-PRS compliant mechanism. Also, a prototype has been tested, using a coordinate measuring machine to verify its dimensions and the resulting displacements in the end effector and the actuated joints. Finally, those measurements have been compared with the FEM and the rigid body kinematics predictions, contrasting the validity of those two modelling approaches for the kinematic design of compliant mechanisms.

**KEYWORDS:** Parallel kinematics; compliant mechanisms; flexure joints design



(Figures and Tables are provided for a better comprehension)

## 1. INTRODUCTION

At present, the requirements of precision and surface finish in different areas as scientific, medical, metrological and communication fields have led to the necessity of creating new mechanisms capable of achieving accuracy constraints on the order of microns or nanometers. A well-known solution for many of these high-tech applications are the compliant mechanisms [1], which allow generating motions with great repeatability, precision, speed and a high bandwidth, through the controlled deformation in several points of their monolithic structure. Those flexible points are flexure joints, that substitute the traditional joints used in typical mechanisms overcoming the problems they usually suffer, as friction, clearances, hysteresis and wear. Nevertheless, the main drawback of these mechanisms is a more complex design, because it is necessary to control the elastic deformation of the joints, and the appearance of parasitic motions together with the desired displacements. For that reason, it is important to develop approaches to study, design and validate these compliant machines, which is one of the objectives of the present work.

Here, the design of a 3-PRS compliant parallel mechanism [2] is proposed. It is a fusion of a parallel mechanism [3–6] and a compliant mechanism, so the advantages of both devices can be obtained: higher mechanical stiffness, higher loading capacity, and higher positioning accuracy from the parallel mechanism and the zero backlash, no friction, no need for lubrication from the flexure devices. The axisymmetric arrangement of a 3-PRS causes that it is a common solution among the compliant parallel mechanisms for precision operations.

As a function of the kinematics of the device and the geometry of the joints, it is possible to create a large number of combinations. An example of a 1 degree of freedom (dof) compliant device is presented by Kim and Choi in [7], that consists of a single-axis flexure-based nano-positioning stage with a range of motion up to a millimeter and a compact stage. A reduction of the parasitic movements and an increase of the accuracy are achieved by means of their process design, providing an optimization of the structure. Others examples of 1 dof compliant devices can be observed in [8–11]. In the same way, it is possible to develop mechanisms with 2 dof, as for example the stage presented by Wang and Han in [12], where the design of a planar motion stage based on flexure elements allows large ranges of motion along x and y direction without causing over-constraint or significant errors. Also, the authors provide some useful steps for designing and analyze by FEM compliant devices. Another case of 2 dof compliant mechanism is presented in [13], where the design of a flexure-based XY stage tries to obtain a relatively large range and high scanning speed device. Its experimental setup and characterization is shown based on the FEM analysis performed. Also, large number of 3 dof mechanisms have been developed in the current literature. For example, an ultra-precision XYθz flexure stage with nanometer accuracy is presented by Kim et al. in [14]. Other sample of this type of devices is shown in [15], where a high-performance three-axis serial-kinematic nano-positioning stage for high-bandwidth applications is presented by Kenton and Leang. Moreover, the necessary steps to achieve a good design, characterization and control are presented. Another 3 dof mechanism is presented in [16], where a XYZ compliant parallel manipulator composed by identical spatial double four-beam modules, is presented. Additional examples of this type of devices are presented in [2,17]. To conclude, some examples of 6 dof mechanisms are indicated. A micro-scale manipulator based on a six-DOF compliant parallel mechanism is presented by Liang et al. [18]. This design is featured by piezo-driven actuators and integrated force sensor capable of delivering six-DOF motions with high precision and providing real-time force information for feedback control. On the other hand, a low stiffness six degrees of freedom compliant precision stage is given in [19]. In it, Dunning et al detail the dimensional optimization of the design and the process of experimental validation of the prototype. Further instances of 6 dof devices are shown in [20,21].

The present work will be focused on the kinematics study, design process, construction and experimental validation of the kinematics of a prototype of the 3-PRS compliant mechanism. Firstly, the proposed design approach is explained and developed in Sections 2 to 5, where the rigid body kinematics of the 3-PRS will be developed, the kinematic requirements for the actuators and joints will be calculated and the design process of the flexible joints by FEM will be explained. Finally, the experimental procedure to verify the kinematics of a developed prototype will be shown. To end up, a discussion about the results reached by the ideal kinematics of a 3-PRS, the FEM kinematics and the prototype will be made.

## 2. PROCEDURE FOR THE KINEMATIC DESIGN

The background of the present work is the development of a hybrid milling machine of 5 degrees of freedom for milling moulds for microlenses, where the spindle is fixed to a portal and the workpiece is

manipulated by a XY stage under a 3-PRS compliant parallel mechanism with direct measurement of the platform position. The milling of microlenses consists on milling a matrix of  $N \times N$  concave aspherical cavities on one face of a cylindrical workpiece of diameters ranging from 10 to 20 mm. The lenses have diameters from 0.5 mm to 2 mm and a sagittal depth less than 1 mm. Hence, in the hybrid manipulator, the XY stage carries out the long travel range in X and Y while the parallel kinematics stage has to provide mainly the Z motion and, if possible, two rotations around X and Y to improve the tool orientation, see Fig. 1. The XY stage also compensates the parasitic motions in X and Y of the parallel kinematics stage.

To obtain the kinematic requirements in terms of displacements needed, a standard milling process has been designed, with a matrix of  $4 \times 4$  cavities in a cylindrical mould of 18 mm. The cavities are spherical with a diameter of 2 mm, and are machined in down-milling with a spiral down strategy in counter-clock direction. The offset between the part and the tool tip for the motions between cavities is of 1mm. As a conclusion, the needed range in X and Y is  $\pm 10$ mm and in Z  $\pm 2$ mm, with the objective of maximize the two rotations as much as possible. As there exists commercial solutions for the XY stage, the final purpose of this work is the design of the compliant parallel stage. A compliant solution has been considered as the structural requirements are not very demanding, given the fact that the estimated cutting forces of the micromilling process are below 1 N, and the travel range can be reached with enough precision. The selection of a 3-PRS is due to its stiffness and thermal properties due to its axisymmetric configuration.

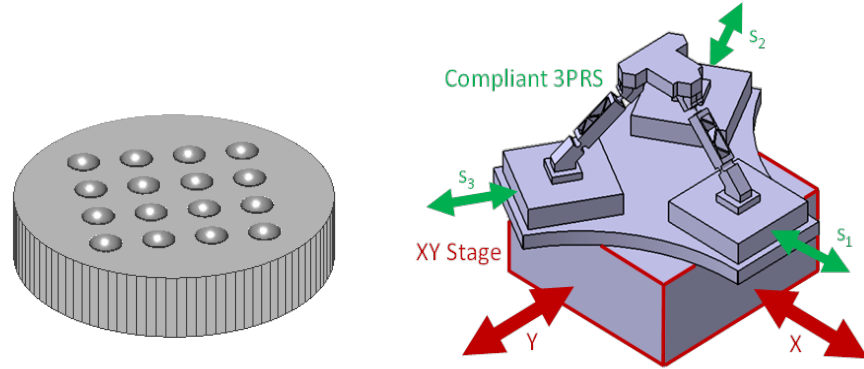


FIGURE 1. WORKPIECE AND SCHEMATIC OF THE HYBRID MANIPULATOR.

Hence, the aim of this study is to achieve the kinematic design of a 3-PRS compliant parallel manipulator capable of performing displacements in Z direction as well as two rotations around X and Y axes. To reach this objective, the following procedure has been developed. Firstly, the rigid body kinematics of the 3-PRS is solved, assuming that under small displacements, there will not appear parasitic translations in the compliant joints that change the rotation center location, hence, the kinematics of the rigid body mechanism will be similar to the compliant one. This assumption is a common practice designing compliant mechanisms [7,17-18]. The rigid body kinematics provides the necessary displacements in the actuators as well as the displacements that the flexure joints must fulfill. Once these requirements are established, it is possible to design the flexure joints by means of an iterative process based on FEM calculations, where the stress in the joints becomes a crucial design parameter. First, the FEM study is applied to an isolated flexure joint, to analyze if provides the demanded displacements, and the behavior of those joints in the whole manipulator are again analyzed by FEM, to reach a homogenous distribution of the stress in all the joints. In the following sections, each of these points will be widely explained, providing the achieved relations, the developments for the design and the validation, and the obtained results, both theoretical as experimental ones.

### 3. RIGID BODY KINEMATICS OF THE 3-PRS

The rigid body kinematics have been solved following the work from [22]. The notation P, R, S denotes prismatic, revolute and spherical joint, respectively. Each limb connects the base to the moving platform by a P joint, an R joint and an S joint in sequence, where the P joint is actuated by a linear actuator. Thus, the moving platform is attached to the base by three identical PRS linkages,  $C_i B_i$ , whose length is  $L$ , see Fig.2. The points  $B_i$  are located in the moving platform in a circumference of radius  $b$ , whose center is defined as point  $P$ . The angles between the legs and the horizontal plane are  $\alpha_i$ , which are equal to  $45^\circ$  in the default position. Three prismatic actuators at  $120^\circ$  are used; being the joint space coordinates  $s_i$ . The location of the actuators in the zero position is defined by the points  $A_i$ , placed on a circle of radius  $a$ , whose center is defined by the point  $O$ .

Two reference systems are defined to solve the kinematics. A fixed frame  $\{x,y,z\}$  is located at point  $O$ , whose X axis is coincident with the slider direction  $OA_1$  and its Z axis is placed vertically. In the same way, a

moving frame  $\{u, v, w\}$  is laid at point P, whose U axis is coincident with the direction  $\mathbf{PB}_1$  and its W axis is perpendicular to the moving platform.

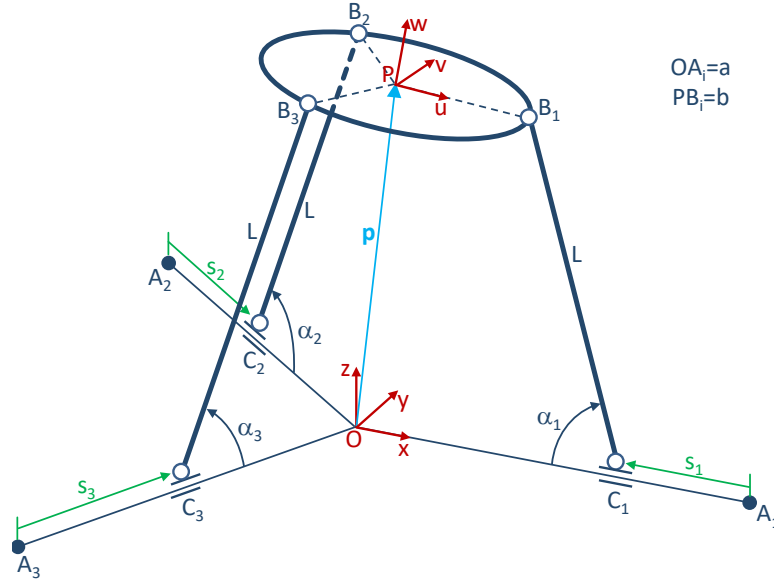


FIGURE 2. SCHEMATIC OF THE 3-PRS MANIPULATOR ANALYZED.

In the following subsections, the motion capabilities and the main parameters of the mechanism will be displayed for a better understanding.

### 3.1 Parasitic movements

The 3-PRS mechanism belongs to the zero torsion parallel mechanisms group [23], and although it is commonly considered as a three degrees of freedom manipulator, that is, translation in Z and rotations around X and Y, the truth is that once a set of input displacements is introduced, in the platform there appear three small coupled motions, two translations in X and Y and a rotation around Z. As they are not the desired degrees of freedom, they are usually called parasitic motions. In this section, these parasitic movements will be calculated as they will be compensated by the XY stage below the parallel manipulator.

To begin with, the position of the center of the moving platform is described by the coordinates  $p_x$ ,  $p_y$ , and  $p_z$ , and its orientation is given by three angles  $\Psi$ ,  $\theta$  and  $\phi$ , which are defined as rotations around the X, Y and Z axes of the fixed frame. Therefore, the position of the center of the moving platform can be expressed as:

$$\mathbf{OP} = \{p_x \quad p_y \quad p_z\}^T \quad (1)$$

On the other hand, the zero position of the actuators in the fixed frame  $\{x,y,z\}$  is defined by:

$$\begin{aligned} \mathbf{OA}_1 &= \{a \quad 0 \quad 0\}^T \\ \mathbf{OA}_2 &= \left\{ -\frac{a}{2} \quad \frac{a\sqrt{3}}{2} \quad 0 \right\}^T \\ \mathbf{OA}_3 &= \left\{ -\frac{a}{2} \quad -\frac{a\sqrt{3}}{2} \quad 0 \right\}^T \end{aligned} \quad (2)$$

Also, it is possible to define the position of the spherical joints in the moving frame  $\{u,v,w\}$  by means of the following relations; where the sub-index 'm' denotes that the vectors are expressed in the moving frame.

$$\begin{aligned}
\mathbf{PB}_{1m} &= \{b \ 0 \ 0\}^T \\
\mathbf{PB}_{2m} &= \left\{-\frac{b}{2} \ \frac{b\sqrt{3}}{2} \ 0\right\}^T \\
\mathbf{PB}_{3m} &= \left\{-\frac{b}{2} \ -\frac{b\sqrt{3}}{2} \ 0\right\}^T
\end{aligned} \tag{3}$$

To transform any vector from the moving frame to the fixed frame, it is necessary to know the rotation matrix  $\mathbf{R}$  that relates both systems, which is expressed as follows:

$$\mathbf{R} = \mathbf{R}_y(\theta)\mathbf{R}_x(\psi)\mathbf{R}_z(\phi) = \begin{bmatrix} u_x & v_x & w_x \\ u_y & v_y & w_y \\ u_z & v_z & w_z \end{bmatrix} = \begin{bmatrix} c\theta c\phi + s\psi s\theta s\phi & -c\theta s\phi + s\psi s\theta c\phi & c\psi s\theta \\ c\psi s\phi & c\psi c\phi & -s\psi \\ -s\theta c\phi + s\psi c\theta s\phi & s\theta s\phi + s\psi c\theta c\phi & c\psi c\theta \end{bmatrix} \tag{4}$$

Where  $c$  stands for cosine and  $s$  refers to the sine. Also,  $u$ ,  $v$  and  $w$  are defined as three unit vectors along the  $U$ ,  $V$  and  $W$  axes of the moving reference system  $P$ .

The position of each spherical joint regarding to the fixed reference system can be expressed as:

$$\mathbf{OB}_i = \mathbf{OP} + \mathbf{R}\mathbf{PB}_{im} \quad i = 1, 2, 3 \tag{5}$$

Developing  $\mathbf{OB}_i$  for each limb, the following three equations are obtained:

$$\begin{aligned}
\mathbf{OB}_1 &= \{p_x + u_x b \quad p_y + u_y b \quad p_z + u_z b\}^T \\
\mathbf{OB}_2 &= \left\{p_x - \frac{u_x b}{2} + \frac{\sqrt{3}v_x b}{2} \quad p_y - \frac{u_y b}{2} + \frac{\sqrt{3}v_y b}{2} \quad p_z - \frac{u_z b}{2} + \frac{\sqrt{3}v_z b}{2}\right\}^T \\
\mathbf{OB}_3 &= \left\{p_x - \frac{u_x b}{2} - \frac{\sqrt{3}v_x b}{2} \quad p_y - \frac{u_y b}{2} - \frac{\sqrt{3}v_y b}{2} \quad p_z - \frac{u_z b}{2} - \frac{\sqrt{3}v_z b}{2}\right\}^T
\end{aligned} \tag{6}$$

The revolute hinges set that the spherical joints can only move in the fixed planes defined by the linear actuators  $\mathbf{OA}_i$  and the legs of the manipulator  $\mathbf{C}_i\mathbf{B}_i$ . Therefore, the following three mechanical constraints are imposed to the mechanism:

$$OB_{1y} = 0 \tag{7}$$

$$OB_{2y} = -\sqrt{3}OB_{2x} \tag{8}$$

$$OB_{3y} = \sqrt{3}OB_{3x} \tag{9}$$

Substituting the expressions of  $\mathbf{OB}_i$  from the Eq. (6) into the Eqs. (7)-(9), and developing these expressions, the following equivalences are reached:

$$p_y = -u_y b \tag{10}$$

$$p_x = \frac{b}{2}(u_x - v_y) \tag{11}$$

$$u_y = v_x \tag{12}$$

Substituting the expressions of  $u_i$  and  $v_i$  from the rotation matrix  $\mathbf{R}$ , in Eq. (4), into Eqs. (10) and (11), the 3-PRS dependent variables or parasitic motions are obtained:

$$\phi = \text{atan} \left( \frac{\sin \psi \sin \theta}{\cos \psi + \cos \theta} \right) \quad (13)$$

$$p_x = \frac{b}{2} (\cos \theta \cos \phi + \sin \psi \sin \theta \sin \phi - \cos \psi \cos \phi) \quad (14)$$

$$p_y = -b \cos \psi \sin \phi \quad (15)$$

From Eq. (13) it can be stated that for small rotations around Z and Y, the parasitic rotation  $\phi$  will be negligible.

### 3.2 Inverse kinematics modeling

The aim of the inverse kinematic problem is to find the values that should take the active joint coordinates of the mechanism  $s_i$ , to reach a given position and orientation of the platform. Firstly, referring to Fig.2, the following relationships can be obtained.

$$\mathbf{A}_i \mathbf{B}_i = \mathbf{OB}_i - \mathbf{OA}_i \quad i = 1, 2, 3 \quad (16)$$

Where  $\mathbf{OB}_i$  and  $\mathbf{OA}_i$  are expressed in Eq. (6) and (2). Also, the expression for  $\mathbf{C}_i \mathbf{B}_i$  can be written as:

$$\mathbf{C}_i \mathbf{B}_i = L \cdot \mathbf{l}_{i0} = \mathbf{A}_i \mathbf{B}_i - \mathbf{A}_i \mathbf{C}_i = \mathbf{A}_i \mathbf{B}_i - s_i \cdot \mathbf{s}_{i0} \quad i = 1, 2, 3 \quad (17)$$

Where  $L$  is the length of the limbs,  $\mathbf{l}_{i0}$  represents the unit vector along the direction of each leg and the unit vectors  $\mathbf{s}_{i0}$  define the positive direction of motion of the actuators and are written as:

$$\mathbf{s}_{i0} = -\frac{\mathbf{OA}_i}{OA_i} \quad i = 1, 2, 3 \quad (18)$$

Rearranging and squaring the components of the Eq. (17), a quadratic equation is found.

$$s_i^2 - 2s_i \cdot \mathbf{s}_{i0} \cdot \mathbf{A}_i \mathbf{B}_i + \mathbf{A}_i \mathbf{B}_i \cdot \mathbf{A}_i \mathbf{B}_i - L^2 = 0 \quad i = 1, 2, 3 \quad (19)$$

Solving Eq. (19) allows us to obtain the solutions for the inverse kinematic problem.

$$s_i = (\mathbf{s}_{i0} \cdot \mathbf{A}_i \mathbf{B}_i) \pm \sqrt{(\mathbf{s}_{i0} \cdot \mathbf{A}_i \mathbf{B}_i)^2 - \mathbf{A}_i \mathbf{B}_i \cdot \mathbf{A}_i \mathbf{B}_i + L^2} \quad i = 1, 2, 3 \quad (20)$$

### 3.3 Passive coordinates

In this subsection, the expressions for the angles of the both joints will be developed to calculate the rotations that are produced in the hinges while the manipulator is performing a programmed operation.

#### 3.3.1 Rotation at revolute joints

The rotation in the revolute joints as consequence of a displacement of the manipulator can be obtained solving the following development. Referring to Fig.2:

$$\mathbf{l}_{i0} = \frac{\mathbf{C}_i \mathbf{B}_i}{L} \quad i = 1, 2, 3 \quad (21)$$

Knowing this information, the angles in the revolute joints can be calculated using the dot product of  $\mathbf{s}_{i0}$  and  $\mathbf{l}_{i0}$ , which have been shown in Eq. (17) and (18).

$$\alpha_i = \text{acos} \left( \frac{\mathbf{l}_{i0} \cdot \mathbf{s}_{i0}}{l_{i0} \cdot s_{i0}} \right) \quad i = 1, 2, 3 \quad (22)$$

#### 3.3.2 Rotation at spherical joints

To study the rotation at the spherical joints, two sets of moving frames have been used. The first set,  $\mathbf{F}_i = \{m_i, n_i, l_i\}$ , will be fixed to the moving platform, and the other,  $\mathbf{F}_{i0} = \{m_{i0}, n_{i0}, l_{i0}\}$ , will move together with the leg. Both have the origin located at the spherical joints  $B_i$  and overlap in the default position, with  $\mathbf{m}_{i0}$  and  $\mathbf{m}_i$  parallel to each revolute joint axis and  $\mathbf{l}_{i0}$  and  $\mathbf{l}_i$  aligned with each limb. A scheme can be seen in Fig. 3 for a pure vertical translation of the moving platform. Rotation angles around the m- and n-axes,  $\beta_{mi}$  and  $\beta_{ni}$ , will make reference to the deflection of the joint and rotation around the l-axis,  $\beta_{li}$ , will be the torsional deformation.

Let's consider here the following four rotation matrices:  $\mathbf{R}_{im}$  to relate  $\mathbf{F}_i$  with  $\{u, v, w\}$ ,  $\mathbf{R}$  mentioned in Eq. (4) to relate  $\{u, v, w\}$  with  $\{x, y, z\}$ ,  $\mathbf{R}_{iSjoint}$  reflects the spherical joints rotation and relates  $\mathbf{F}_i$  with  $\mathbf{F}_{i0}$ , and  $\mathbf{R}_{iRjoint}$  reflects the revolute joints rotation and relates  $\mathbf{F}_{i0}$  with  $\{x, y, z\}$ . They meet the following relation:

$$\mathbf{R}_{iRjoint} \cdot \mathbf{R}_{iSjoint} = \mathbf{R} \cdot \mathbf{R}_{im} \quad i = 1, 2, 3 \quad (23)$$

Hence, to obtain the spherical joint rotation, the angles between frames  $\mathbf{F}_i$  and  $\mathbf{F}_{i0}$  must be calculated, which means calculating  $\mathbf{R}_{iSjoint}$  as a function of the other matrices:

$$\mathbf{R}_{iSjoint} = \mathbf{R}_{iRjoint}^T \cdot \mathbf{R} \cdot \mathbf{R}_{im} \quad i = 1, 2, 3 \quad (24)$$

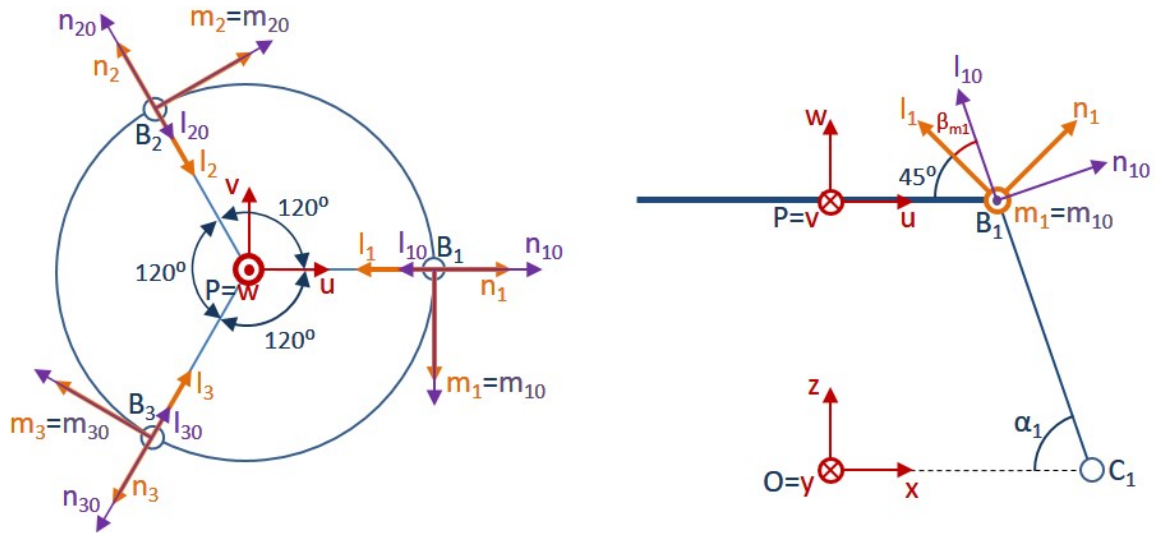


FIGURE 3. REFERENCE SYSTEMS FOR THE SPHERICAL JOINTS ROTATION STUDY.

To do that, first, vectors  $\mathbf{m}_{i0}$  are developed as the characteristic vectors of the three planes at  $120^\circ$  that constrain the motion of each leg to each plane.

$$\begin{aligned} \mathbf{m}_{10} &= \{0 \quad -1 \quad 0\}^T \\ \mathbf{m}_{20} &= \left\{ \frac{\sqrt{3}}{2} \quad \frac{1}{2} \quad 0 \right\}^T \\ \mathbf{m}_{30} &= \left\{ \frac{-\sqrt{3}}{2} \quad \frac{1}{2} \quad 0 \right\}^T \end{aligned} \quad (25)$$

Unit vectors  $\mathbf{l}_{i0}$  are calculated as shown in Eq. (21). Finally, the unit vectors  $\mathbf{n}_{i0}$  can be obtained by means of the cross product of  $\mathbf{l}_{i0}$  and  $\mathbf{m}_{i0}$ .

$$\mathbf{n}_{i0} = \mathbf{l}_{i0} \wedge \mathbf{m}_{i0} \quad i = 1, 2, 3 \quad (26)$$

As a result, the rotation matrices  $\mathbf{R}_{iRjoint}$  that relate the frames of the legs  $\mathbf{F}_{i0}$  with the global reference system  $\{x, y, z\}$  are:

$$\mathbf{R}_{iRjoint} = [\mathbf{m}_{i0} \quad \mathbf{n}_{i0} \quad \mathbf{l}_{i0}] \quad i = 1, 2, 3 \quad (27)$$

On the other hand, the rotation matrices  $\mathbf{R}_{im}$ , that relate  $\mathbf{F}_i$  and  $\{u, v, w\}$  systems, are calculated. The unit vectors for each system  $\mathbf{F}_i$  can be defined by the following expressions in the moving frame:

$$\begin{aligned} \mathbf{m}_{1m} &= \{0 \quad -1 \quad 0\}^T \\ \mathbf{n}_{1m} &= \{\sin\alpha_0 \quad 0 \quad \cos\alpha_0\}^T \\ \mathbf{l}_{1m} &= \{-\cos\alpha_0 \quad 0 \quad \sin\alpha_0\}^T \end{aligned} \quad (28)$$

$$\begin{aligned} \mathbf{m}_{2m} &= \left\{ \frac{\sqrt{3}}{2} \quad \frac{1}{2} \quad 0 \right\}^T \\ \mathbf{n}_{2m} &= \left\{ \frac{-\sin\alpha_0}{2} \quad \frac{\sqrt{3}\sin\alpha_0}{2} \quad \cos\alpha_0 \right\}^T \\ \mathbf{l}_{2m} &= \left\{ \frac{\cos\alpha_0}{2} \quad \frac{-\sqrt{3}\cos\alpha_0}{2} \quad \sin\alpha_0 \right\}^T \end{aligned} \quad (29)$$

$$\begin{aligned} \mathbf{m}_{3m} &= \left\{ -\frac{\sqrt{3}}{2} \quad \frac{1}{2} \quad 0 \right\}^T \\ \mathbf{n}_{3m} &= \left\{ \frac{-\sin\alpha_0}{2} \quad \frac{-\sqrt{3}\sin\alpha_0}{2} \quad \cos\alpha_0 \right\}^T \\ \mathbf{l}_{3m} &= \left\{ \frac{\cos\alpha_0}{2} \quad \frac{\sqrt{3}\cos\alpha_0}{2} \quad \sin\alpha_0 \right\}^T \end{aligned} \quad (30)$$

Being  $\alpha_0=45^\circ$  the default value of  $\alpha_i$  in the proposed case of study. Hence, each rotation matrix  $\mathbf{R}_{im}$  has the following expression:

$$\mathbf{R}_{im} = [\mathbf{m}_{im} \quad \mathbf{n}_{im} \quad \mathbf{l}_{im}] \quad i = 1, 2, 3 \quad (31)$$

Substituting Eq. (31), Eq. (27) and Eq. (4) in Eq. (24),  $\mathbf{R}_{iSjoint}$  is obtained. On the other hand, this matrix can be developed as a function of three rotations around all the axes system  $\mathbf{F}_{i0}$ :  $\beta_{mi}$ ,  $\beta_{ni}$ , and  $\beta_{li}$ , see Fig. 4. The sequence consists of a rotation around the m-axis, followed by a rotation around the n-axis and ending with a rotation around the l-axis. Therefore, the rotation matrix that relates the systems  $\mathbf{F}_i$  with  $\mathbf{F}_{i0}$  may also be expressed as the product of the above rotation matrices.

$$\mathbf{R}_{iSjoint} = \mathbf{R}_{mi}\mathbf{R}_{ni}\mathbf{R}_{li} = \begin{bmatrix} c\beta_{ni}c\beta_{li} & -s\beta_{ni}s\beta_{li} & s\beta_{ni} \\ s\beta_{mi}s\beta_{ni}c\beta_{li} + c\beta_{mi}s\beta_{li} & -s\beta_{mi}s\beta_{ni}s\beta_{li} + c\beta_{mi}c\beta_{li} & -s\beta_{mi}c\beta_{ni} \\ -c\beta_{mi}s\beta_{ni}c\beta_{li} + s\beta_{mi}s\beta_{li} & c\beta_{mi}s\beta_{ni}s\beta_{li} + s\beta_{mi}c\beta_{li} & c\beta_{mi}c\beta_{ni} \end{bmatrix} \quad (32)$$

Equating the terms of the matrices in Eq. (24) and (32), the rotations in the spherical joints are obtained:



$$\begin{aligned}
\beta_{mi} &= \text{atan}\left(\frac{-\mathbf{R}_{i-i0}(2,3)}{\mathbf{R}_{i-i0}(3,3)}\right) \quad i = 1, 2, 3 \\
\beta_{ni} &= \text{asin}(\mathbf{R}_{i-i0}(1,3)) \\
\beta_{ii} &= \text{atan}\left(\frac{-\mathbf{R}_{i-i0}(1,2)}{\mathbf{R}_{i-i0}(1,1)}\right)
\end{aligned} \tag{33}$$

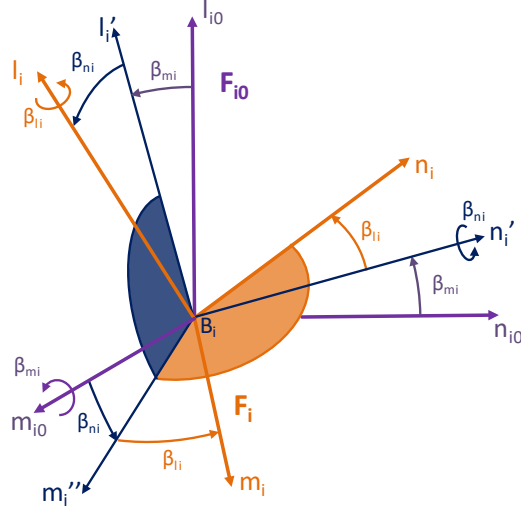


FIGURE 4. ROTATIONS PERFORMED BETWEEN SYSTEMS  $F_i$  AND  $F_{i0}$ .

### 3.4 Forward kinematics modeling

The forward kinematic problem determines the position and orientation of the platform with respect to the fixed frame, when the values of the actuated joints are known. Referring to Fig.2, the following equivalences can be obtained by imposing a fixed length,  $L$ , for each limb of the mechanism:

$$\mathbf{OB}_i - \mathbf{OC}_i = \mathbf{OB}_i - (\mathbf{OA}_i + \mathbf{AC}_i) = \mathbf{C}_i \mathbf{B}_i \quad i = 1, 2, 3 \tag{34}$$

$$|\mathbf{OB}_i - \mathbf{OC}_i|^2 = L^2 \tag{35}$$

The developed expressions can be observed in the **Appendix A**. The previous calculated relationships together with the equations Eq.(13)-(15) form a system of six equations which must be solved. As inputs for the system, the displacements of the actuators,  $\mathbf{s}_i$ , and the initial position of the platform  $\{p_{x0}, p_{y0}, \phi_0\}$  are introduced. By means of an algebraic-loop solver in Matlab Simulink, the real position of the platform  $p_s, \Psi, \theta$  is calculated. These solutions will be used as direct feedback to the resolution process, see Fig. 5.

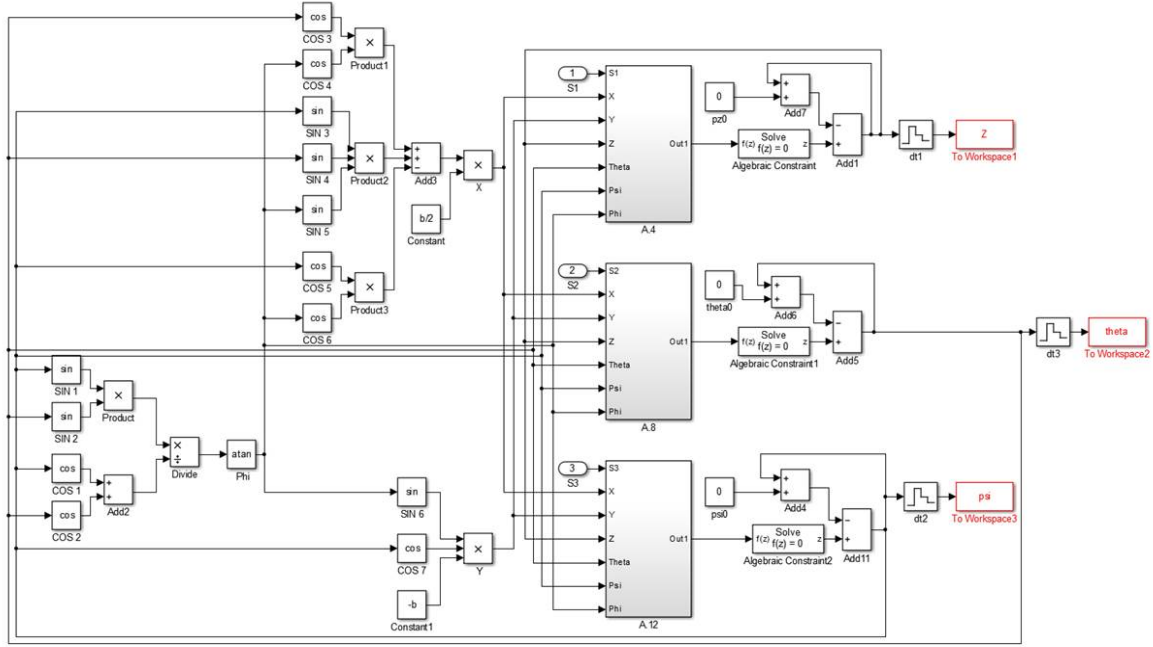


FIGURE 5. FORWARD KINEMATIC RESOLUTION SCHEME.

#### 4. JOINT REQUIREMENTS

As stated in Section 2, the compliant 3-PRS must be able to achieve a Z travel of  $\pm 2\text{mm}$ . With regard to the rotations around the X and Y axes, an objective has been set in ensuring minimum values of  $\pm 0.2^\circ$  over the entire range of Z. After taking into account the whole footprint of the hybrid manipulator, the modal frequencies and the minimum static stiffness needed in the platform to minimize the legs deflection due to the cutting forces, the dimensions selected for the prototype are a length L of the legs of 109.215 mm, measured between the center points of the two flexure stages, a distance b from the platform axis to the center of the spherical joints of 47.91mm, and a value of  $45^\circ$  for the three passive angles  $\alpha$  in the default position. With  $45^\circ$ , no amplification happens, so the prismatic joints actuators must provide at least a travel range of  $\pm 2\text{mm}$ . The section of the legs is  $10 \times 10 \text{ mm}^2$ . An aluminum alloy 7075 with a Young modulus of 72 GPa, a Poisson's ratio of 0.33 and a density of  $2.81\text{g/cm}^3$  has been used for the first prototype.

These requirements have been introduced in the inverse kinematics problem (IKP) and the displacements on the actuators and the passive angles in the joints have been calculated. In Fig. 6, the studied positions are shown. As it can be seen in the first three graphs, the IKP has been solved with all the possible combinations of a Z displacement of  $\pm 2\text{mm}$  and rotations  $\psi$  and  $\theta$  of  $\pm 0.2^\circ$ . As a result, the required displacements of the actuated joints,  $s_i$ , are achieved. They are comprised between  $-2.15\text{mm}$  and  $2.30\text{mm}$ , see the fourth graph of Fig. 6. With regard to the rotation of the revolute joints,  $\alpha_i$  must reach a variation of  $\pm 1.7^\circ$  and regarding the rotations in the spherical hinges, the angles that must be reached are  $\beta_m = \pm 1.9^\circ$ ,  $\beta_n = \pm 0.2^\circ$  and  $\beta_l = \pm 0.2^\circ$ , see Fig. 7.

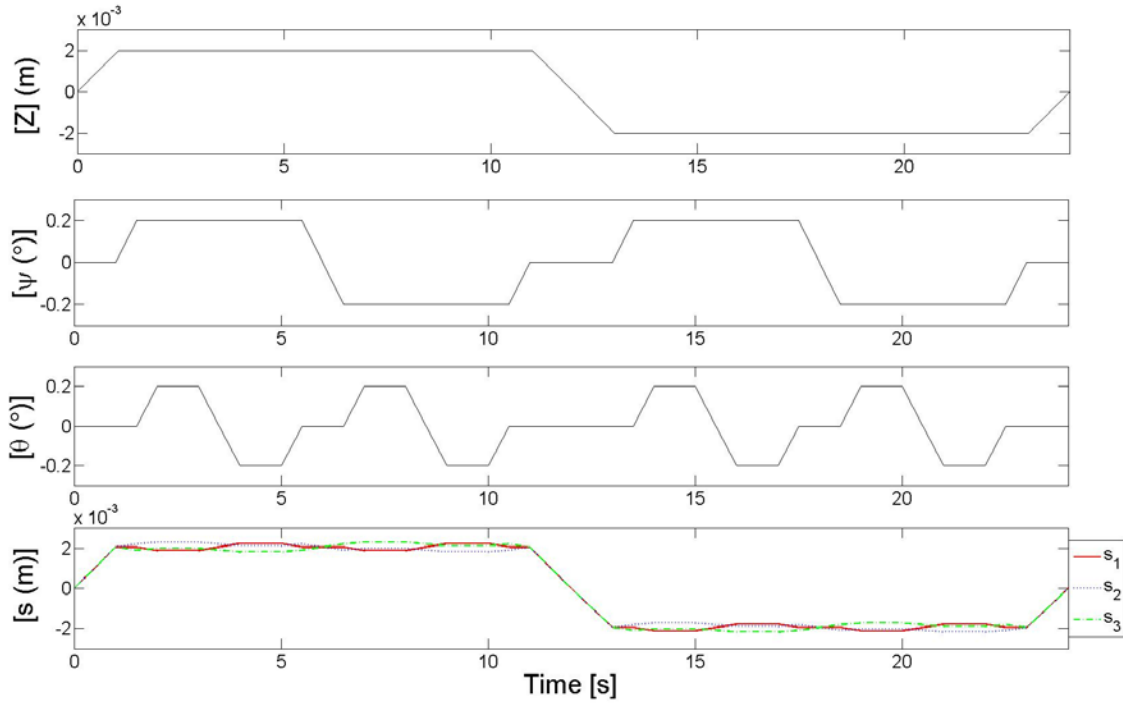


FIGURE 6. MOVEMENTS ON THE PLATFORM ( $z$ ,  $\psi$ ,  $\theta$ ) AND DISPLACEMENTS IN THE ACTUATORS ( $s_i$ ).

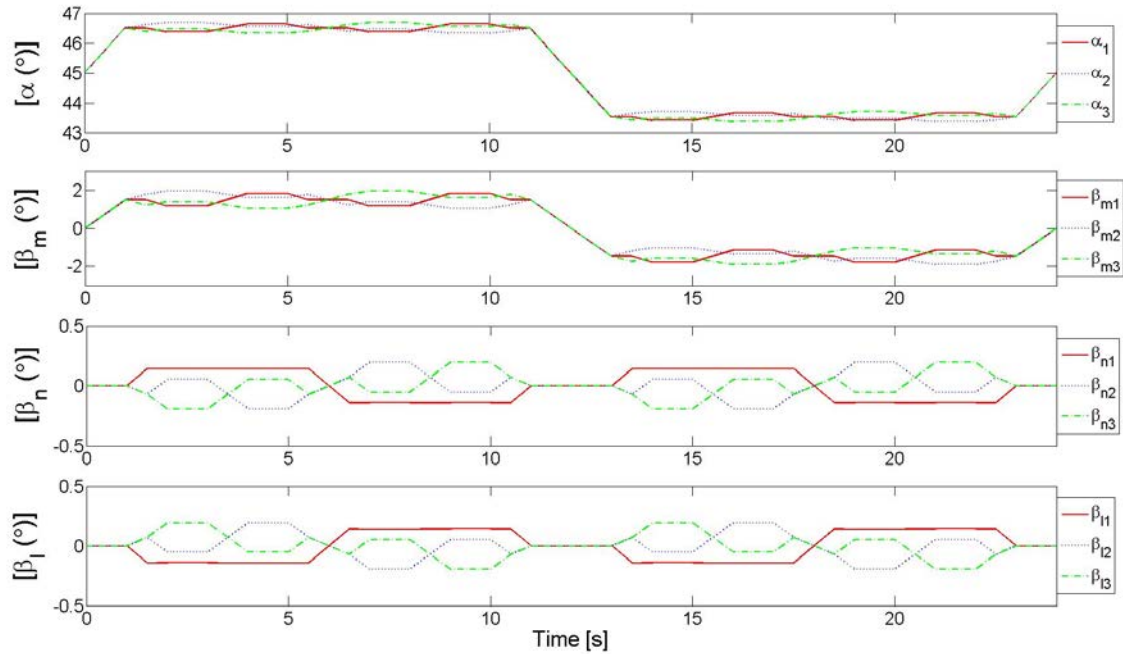


FIGURE 7. ROTATIONS IN REVOLUTE JOINTS ( $\alpha_i$ ) AND IN SPHERICAL JOINTS ( $\beta_{mi}$ ,  $\beta_{ni}$ ,  $\beta_{li}$ ).

### 5. FEM BASED DESIGN OF THE 3-PRS COMPLIANT MECHANISM JOINTS

To design and analyze the performance of the prototype, simulations using ANSYS Workbench FEM software have been made and the main features of the flexure stage have been obtained. In Fig. 8 an example of the designed stage and the mesh is shown. The mesh applied to the mechanism consists of a tetrahedral mesh. The nodes size in the flexure joints has been reduced with a ratio 10:1 respect to the whole structure to obtain

more accurate results in the areas with a high deformation and stress concentration. Quadratic tetrahedrons have been used for the mesh.

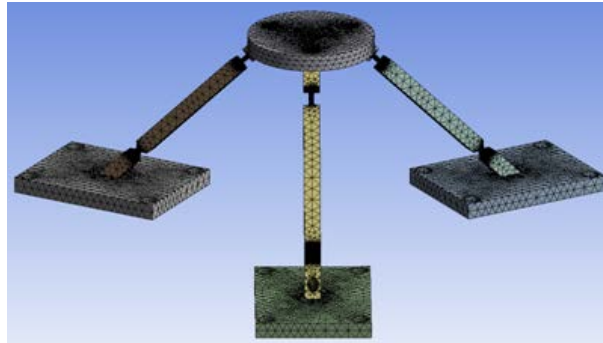


FIGURE 8. 3-PRS COMPLIANT MECHANISM MODEL.

To obtain the final dimensions of the flexure joints, an optimization process has been developed. The first step has been to know the displacement requirements of the joints by means of the inverse kinematics, as explained in section 3. Once this information is known, the design of the joints can be done[24], attending to the following conditions: a) the joints must be able to achieve the required movements, and b) the maximum stress has to be controlled to not enter in the plastic zone. The Al 7075 tensile yield strength is equal to 503 MPa. A safety factor has been established, so a stress greater than 400 MPa has not been overcome.

To characterize the revolute hinge, one side has been fixed and a moment has been applied in the other side. For the spherical joint, as in the previous case, one side has been fixed and two moments have been applied in the other side. In both cases, the fixed side and the applied loads have been located at a distance of 20mm from the compliant bodies [25]. The aim is to avoid local disturbances by the boundary conditions in the points where the measurements have been performed and therefore, a reduction in the accuracy of the results. With these configurations, it is possible to measure both the maximum stresses and displacements supported in the joints, see Fig. 9.

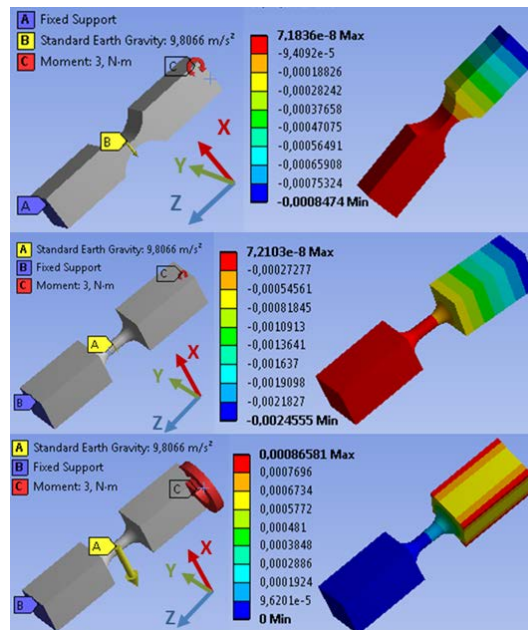


FIGURE 9. LOADING AND DEFORMATION OF THE JOINTS. ABOVE: BENDING OF THE REVOLUTE JOINT; MIDDLE AND BELOW: BENDING AND TORSION OF THE SPHERICAL JOINT.

Once the potential joints are obtained, they are introduced in the whole structure. It should be noted that their behaviour can vary when they are subjected to the working conditions of the mechanism. For that reason,

the next step has been to calculate the features of the whole structure. A static structural analysis has been performed, applying several force steps in the place of the actuators. Thanks to this, the relations between the applied forces and movements in the actuators and the displacements on the platform have been calculated. What is more, the maximum stress in the structure, which occurs in one of the flexure joints, has been controlled to avoid exceeding a stress greater than 400 MPa, as in the joints design. Also the maximum stresses supported in the hinges have been controlled to achieve similar values in both revolute and spherical joints. The objective is to avoid weaknesses in the structure due to higher efforts on specific type of compliant hinge, see Fig.10. A relation between the maximum stresses supported in the joints comprised between  $1 \pm 0.2$  has been established as a design condition. Regarding the computational time, an average joint analysis has taken 384.3 s and an average analysis for the whole manipulator has taken 3846.2 s with an Intel-Core i5-2430M with 2.4 GHz and 6GB of RAM.

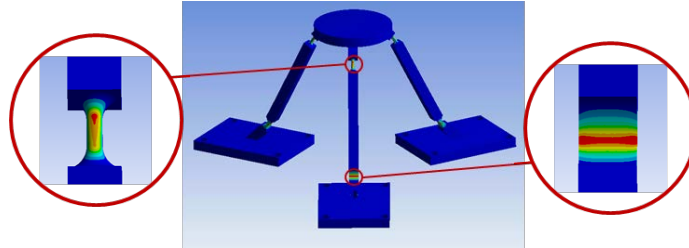
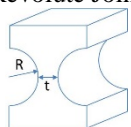
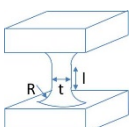


FIGURE 10. STRESSED AREAS OF THE JOINTS DURING A Z DISPLACEMENT.

As design parameters, the radius and thickness for the revolute joints, and radius, thickness and length for the spherical joints have been chosen. Depending of the variation of any of these items, new features in the mechanism can be obtained. From the authors experience designing a compliant 3-PRS, the influences of all of them have been determined. Some useful indications to get a new mechanism  $i+1$  starting from a previous case design  $i$  are shown in Table 1. As can be seen, for instance, an increase in the thickness of the revolute joint causes a significant increment in the stiffness of the structure, by a factor greater than 1.5, while the Z displacement and the relation of maximum stresses in the joints suffer a slighter reduction with a factor of 0.8. By contrast, an increase in the length of the spherical joint causes a tinier reduction of the structural stiffness, an important increase of the Z displacement and a notable reduction of the relation of maximum stresses.

	Positive increase	Structural Stiffness ( $\eta_{i+1}/\eta_i$ )	Displacement Z direction ( $d_{i+1}/d_i$ )	Relation Max. Stress in joints ( $T_{i+1}/T_i$ ) where $T = T_{sph}/T_{rev}$
Revolute Joint 	$t_{rev}$	↑ ↑ ↑	↓	↓
	$R_{rev}$	↓	↑	↑ ↑
Spherical Joint 	$t_{sph}$	↑	↓	↑
	$R_{sph}$	↓	↑ ↑	↓ ↓
	$l_{sph}$	↓	↑ ↑ ↑	↓ ↓ ↓

↑	$\in 1 - 1.2$
↑ ↑	$\in 1.2 - 1.5$
↑ ↑ ↑	$> 1.5$
↓	$\in 0.8 - 1$
↓ ↓	$\in 0.5 - 0.8$
↓ ↓ ↓	$< 0.5$

TABLE 1. INFLUENCE OF THE DESIGN PARAMETERS IN THE STRUCTURE.

Different radii, lengths and thicknesses have been applied to the revolute and spherical flexure joints to obtain the desired motions in the platform and to fulfill the imposed conditions. An iterative process has been developed and as a result, the optimal structure has been obtained. The diagram illustrating the design process can be observed in Fig. 11.

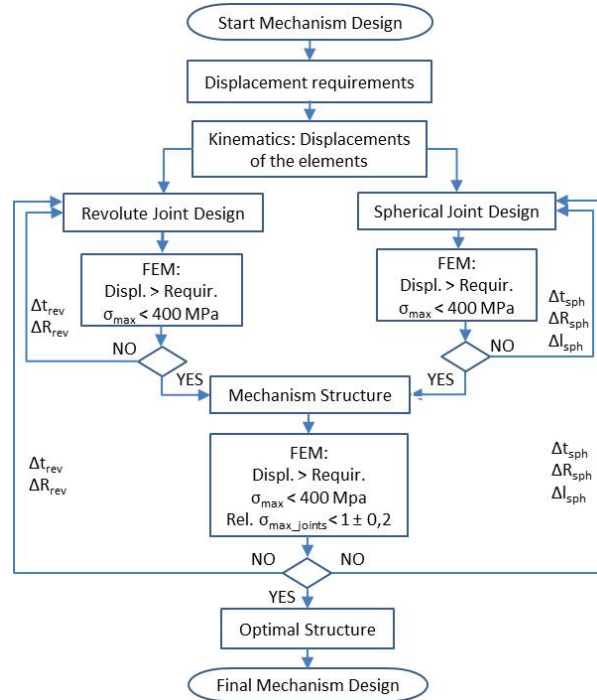


FIGURE 11. SCHEME OF THE DESIGN PROCESS.

For the revolute hinge, the achieved values have been  $R_{rev}=8\text{mm}$  and  $t_{rev}=2\text{mm}$ . Measuring the deformation produced in the joint, the rotational stiffness around the Y axis is  $K_{R_{rev}} = 98.37 \text{ Nm/rad}$ . For the spherical joint, the selected dimensions have been  $l_{sph}=5\text{mm}$ ,  $t_{sph}=3\text{mm}$  and  $R_{sph}=4\text{mm}$ . Also, the flexural stiffness and the torsional stiffness are  $K_{R_{sph}}=32.67\text{Nm/rad}$  and  $K_{T_{sph}}=24.46\text{Nm/rad}$ .

As an example, for a Z displacement of the platform, the obtained results in FEM analysis are shown in Table 2. Some force steps have been applied to the actuators and the occurred displacements in them and on the platform, and the maximum stress in the mechanism have been measured. Attending to the linear behaviour of the values, for a stress of 400MPa, a displacement in z direction equal to 2.205mm should be achieved.

Actuator 1	$F_1$ (N)	20	40	60
	$s_1$ (mm)	0.935	1.899	2.865
Actuator 2	$F_2$ (N)	20	40	60
	$s_2$ (mm)	0.935	1.899	2.865
Actuator 3	$F_3$ (N)	20	40	60
	$s_3$ (mm)	0.935	1.899	2.865
Platform	$z$ (mm)	0.933	1.896	2.859
Joints	Max. stress (MPa)	169.25	344.01	518.78

TABLE 2. STATIC FORCES, DISPLACEMENTS AND STRESS AT THE JOINTS.

## 6. EXPERIMENTAL METHODOLOGY

To validate experimentally the results obtained in the previous sections, a prototype has been built, see Fig.12. The actuation system of the mechanism consists of three identical actuators based on a RE-40 Maxon DC motor with a GP-32A gearbox of 14:1 gear ratio. Flexible couplings are used to connect the output shafts of the gearboxes to three Igus ZLW-1040-02-S-100 linear belt drives.

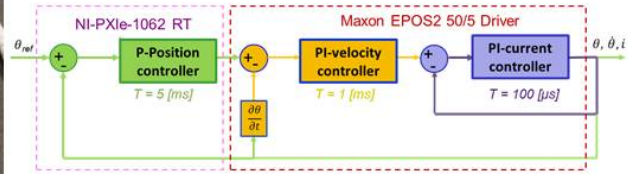
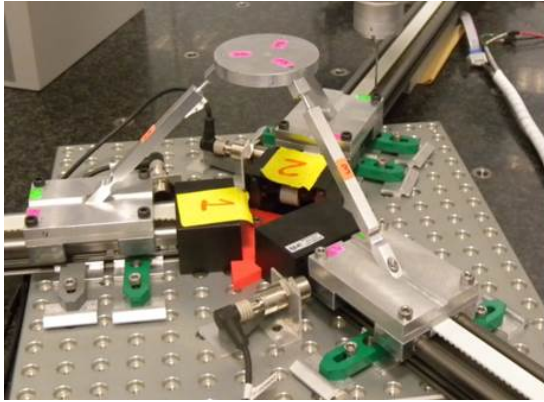


FIGURE 12. LEFT) DEVELOPED PROTOTYPE; RIGHT) CONTROL ARCHITECTURE FOR THE MOTOR OF THE ACTUATION SYSTEM.

Regarding the control of the device, a PID cascaded position, velocity and current control has been used, see Fig. 11. The position is controlled in the first stage on a NI-PXIe 1032 with a Real-Time operating system. The position control loop is based on a proportional gain with a value of  $2.5s^{-1}$  and a 5ms cycle time. The velocity reference, which is the output of this stage, is sent to the motor driver Maxon EPOS2 50/5 through a CANOPEN interface, where the velocity and current regulation is performed. As for the velocity control loop, a PI velocity regulator is employed, whose proportional gain value is of  $0.9Arad^{-1}$  and the integral gain is of  $0.001 Asrad^{-1}$ , and 1ms has been established as cycle time. A current reference, that is the output of the velocity controller, is handled by a PI current controller. The torque constant of the RE-40 motors is  $30.2 \times 10^{-3} Nm/A$ . The end platform position commands are converted to a  $\theta$  reference into the motors using the IKP and the  $\theta$  control is performed. To measure the real position of the manipulator, an external position measuring device has been used, that is, a coordinate measuring machine (CMM) ZEISS MC850 with software ZEISS CALYPSO.

### 6.1 Dimensional verification

Here, the default position of all components has been measured [26]. The selected measurements to perform have been: 1) angles between the guides, Fig.1:  $OA_i-OA_{i+1}$ ; 2) position and orientation of each base, Fig.1: points C; 3) heights and overhead planes of legs, Fig.1:  $L_i \cdot \sin\alpha_0$ ; 4) position and orientation of the platform, Fig.1: point P; and actuators position, Fig.1: points  $A_i$ . In the following paragraphs, the procedure to obtain all of them is explained.

Firstly, the angular position between the guides in XY plane was obtained. To do that, several points on each side of the guides were measured at the same height, as can be seen in Fig. 13. With the coordinates of these points, two equations for each guide were obtained, providing the angles between the guides. The measured angles can be observed in Table 3.

Secondly, the position and orientation of each base was measured. The purpose was to know if the supports where the legs of the prototype were attached were in the same plane, see Fig. 13. The reference plane (RF) to measure was placed on the surface of the CMM to avoid possible inclinations. Several points in each base were measured to obtain the average height and the plane in which were located. With these planes, tilt and location errors could be accounted. In Table 3, the heights and the angles around the X and Y axes of each base are shown. The average height of them is 77.472 mm. It will be necessary to calculate the height of the prototype.





FIGURE 13. DIMENSIONAL VERIFICATION.

Thirdly, the prototype was assembled without the upper platform and the heights and the overhead planes of the legs were measured, see Fig. 13. The average height of each leg can be observed in Table 3. The next step was to perform the complete assembly of the prototype and measure both the height and the inclination of the platform. To do that, several points were measured in the upper surface and in the contour of the platform, see Fig.13, and the plane surface and the axis of the cylinder of the platform were obtained. Intersecting these two elements, the coordinate center and the height of this point were obtained. Also, knowing the equation of the plane, the inclination of the platform around the X and Y axes is determined. These results are shown in Table 3.

Finally, the position of the actuators relative to the fixed frame was also measured. These values allow knowing the real displacements of the actuators when a movement is programmed to the mechanism. To do that, the backplane location of each base was measured, see Fig. 13. Knowing the equations of the planes and the place of coordinate center, the position of the actuators can be achieved. These magnitudes can be observed in Table 3.

GUIDES			BASIS						
Axes	Angles		Plane	Height		$\psi$		$\theta$	
	Design	Error		Design	Error	Design	Error	Design	Error
OA <sub>1</sub> -OA <sub>2</sub>	120°	-0° 5' 24"	C1	77.500	-0.080	0°	-0° 0' 3"	0°	-0° 0' 10"
OA <sub>2</sub> -OA <sub>3</sub>	120°	-0° 1' 12"	C2	77.500	-0.343	0°	0° 23' 49"	0°	-0° 9' 21"
OA <sub>3</sub> -OA <sub>1</sub>	120°	0° 3' 0"	C3	77.500	0.338	0°	0° 17' 34"	0°	0° 15' 25"
<b>LEGS</b>						<b>ACTUATORS</b>			



Leg	Height to RF		Leg height		Actuator	Plane $A_i$		
	Design	Error	Design	Error		Design	Error	
$H_{leg1}$	189,728	-0.031	112.228	0.049	Act. 1	194.232	0.069	
$H_{leg2}$	189,728	0.478	112.228	0.822	Act. 2	194.232	0.069	
$H_{leg2}$	189,728	0.822	112.228	0.484	Act. 3	194.232	0.265	
PLATFORM								
Plane	Height to RF		Prototype height		$\psi$		$\theta$	
	Design	Error	Design	Error	Design	Error	Design	Error
P	197.228	0.136	119.728	0.164	0°	0° 2' 9"	0°	0° 7' 48"

TABLE 3. DIMENSIONAL VERIFICATION RESULTS. DISTANCES IN MILLIMETERS ANGLES IN DMS NOTATION.

In view of the results, the average deviations have been:  $\epsilon_{O_{Ai}-O_{Ai+1}}=0^{\circ}3'12''$  in the angles between the guides;  $\epsilon_c=0.254\text{mm}$ ,  $\epsilon_{\psi_c}=0^{\circ}14'3''$  and  $\epsilon_{\theta_c}=0^{\circ}8'19''$  in the position and orientation of the basis;  $\epsilon_{L.\sin\alpha}=0.452\text{mm}$  in the height of the legs;  $\epsilon_A=0.134\text{mm}$  in the position of the actuators, and  $\epsilon_p=0.164\text{mm}$ ,  $\epsilon_{\psi_p}=0^{\circ}2'9''$  and  $\epsilon_{\theta_p}=0^{\circ}7'48''$  in the position and orientation of the platform. These differences between the design parameters and the real values are due to the introduced errors during the manufacturing and assembly of the prototype. All of them will be considered as starting errors in the following developments because a positioning error is introduced in the mechanism due to these deviations with regard to the design parameters.

## 6.2 Kinematics verification

Here, a series of movements were programmed and the real displacements at the platform and actuators were measured by means of the CMM measuring external device. Two movements in the positive direction of the actuator and other two movements in the negative direction were scheduled.

To perform this task, it was necessary to measure several points on the top surface of the end platform and in the backplane of each base. Knowing the default position of the prototype and the planes containing these measured points and their position, the real displacement and rotation of the platform and the displacements of the actuators were achieved.

In Table 4, in the first three columns, the real displacements  $\Delta s_1$ ,  $\Delta s_2$ ,  $\Delta s_3$ , are shown. These measured movements in the actuators were introduced in a FEM analysis of the prototype. As a result, the displacements on the platform during the FEM analysis,  $z_{FEM}$ ,  $\psi_{FEM}$ ,  $\theta_{FEM}$ , were compared with those measured with the CMM,  $z_{CMM}$ ,  $\psi_{CMM}$ ,  $\theta_{CMM}$ . Also, to check the validity of the rigid body kinematics, the real displacements of the actuators have also been introduced into the forward kinematic problem (FKP) and its solutions,  $z_{FKP}$ ,  $\psi_{FKP}$ ,  $\theta_{FKP}$ , have been compared with the measurements from the CMM. All the results can be observed in Table 4.

$\Delta s$ ( $\mu\text{m}$ )			$\Delta z$ ( $\mu\text{m}$ )			$\Delta\psi$ (DMS)			$\Delta\theta$ (DMS)		
$\Delta s_1$	$\Delta s_2$	$\Delta s_3$	CMM	FEM	FKP	CMM	FEM	FKP	CMM	FEM	FKP
1395	1531	1306	1471	1408	1384	7'47"	4'5"	8'59"	5'13"	0'33"	1'4"
777	685	725	714	727	722	2'41"	-0'45"	-1'38"	0'16"	-1'30"	-3'23"
-676	-494	-706	-636	-624	-631	-2'17"	3'53"	8'55"	-3'34"	1'35"	3'41"
-1485	-1175	-1781	-1437	-1478	-1511	9'8"	11'5"	26'6"	4'21"	0'6"	0'11"

TABLE 4. COMPARISON OF CMM, FEM AND FKP MEASUREMENTS.

In Table 5, the absolute errors of the FEM and FKP predictions regarding the CMM measurements are shown. Comparing the position of the end platform measured by the CMM and the FEM predictions, the linear errors in Z direction are always under 70 microns, and the angular errors are less than 7', see Table 5. Also, while the linear error is somewhat proportional to the displacement, growing for higher displacements, the angular error behavior is more erratic. Due to the fact that the deformation of the mechanism is relatively small and linear, the Z displacement is a 1,3% of the length of the limbs, the FEM estimations calculated with a static analysis should be considered as a good reference, being the main uncertainty the quality of the mesh and the

parameters of the material. So, the deviations observed can be attributed mainly to the measured errors in the prototype due to the manufacturing and assembling stage.

Comparing the CMM measurements with the FKP predictions, similar trends are observed. However, it must be noted that the linear error in Z grows even higher for larger displacements. It is something predictable, as the hypothesis of considering the kinematics of the compliant mechanism as equal to a conventional one is known to lose validity for larger deformations of the flexure joints. Due to the length of the spherical joints, their deflection in large displacements introduces not only a rotation around their central point, but also a translation of the central point itself, which is not considered in the rigid body kinematics. Here, the limit for that hypothesis is observed to be around the millimeter in Z displacement, approximately a 0.9% of the length of the limbs. Below that limit, it must be noted that the error of the FKP predictions in Z translation is always below 10 microns, very close to the predictions of the FEM.

$\Delta z$ ( $\mu\text{m}$ )			$\Delta\psi$ (DMS)			$\Delta\theta$ (DMS)		
CMM	FEM	FKP	CMM	FEM	FKP	CMM	FEM	FKP
	$ \epsilon_{\text{abs}} $	$ \epsilon_{\text{abs}} $		$ \epsilon_{\text{abs}} $	$ \epsilon_{\text{abs}} $		$ \epsilon_{\text{abs}} $	$ \epsilon_{\text{abs}} $
1471	<b>63</b>	<b>87</b>	7'47"	<b>3'42"</b>	<b>1'12"</b>	5'13"	<b>4'40"</b>	<b>4'9"</b>
714	<b>13</b>	<b>8</b>	2'41"	<b>3'25"</b>	<b>4'18"</b>	0'16"	<b>1'46"</b>	<b>3'39"</b>
-636	<b>12</b>	<b>5</b>	-2'17"	<b>6'11"</b>	<b>11'12"</b>	-3'34"	<b>5'9"</b>	<b>7'15"</b>
-1437	<b>41</b>	<b>74</b>	9'8"	<b>1'57"</b>	<b>16'58"</b>	4'21"	<b>4'15"</b>	<b>4'10"</b>

TABLE 5. ABSOLUTE ERRORS IN THE CMM MEASUREMENTS COMPARED TO THE FEM AND FKP PREDICTIONS.

In order to avoid the prototype imperfections in the calculations, it is possible to consider the FEM predictions as optimal results to verify the FKP solutions. The comparison between both cases is shown in Table 6. As it was commented previously, similar results are obtained for small displacements, with deviations fewer than  $8\mu\text{m}$  for Z displacements, increasing these differences when the introduced movements are larger. Therefore, the validity of the FKP model for designing a 3-PRS compliant parallel mechanism under small displacements is demonstrated, and the limit for its assumptions can be quantified in a 0.9% of the length of the limbs.

$\Delta z$ ( $\mu\text{m}$ )		$\Delta\psi$ (DMS)		$\Delta\theta$ (DMS)	
FEM	FKP	FEM	FKP	FEM	FKP
	$ \epsilon_{\text{abs}} $		$ \epsilon_{\text{abs}} $		$ \epsilon_{\text{abs}} $
1408	<b>24</b>	4'5"	<b>4'54"</b>	0'33"	<b>0'31"</b>
727	<b>5</b>	-0'45"	<b>0'53"</b>	-1'30"	<b>1'53"</b>
-624	<b>7</b>	3'53"	<b>5'2"</b>	1'35"	<b>2'6"</b>
-1478	<b>33</b>	11'5"	<b>15'1"</b>	0'6"	<b>0'5"</b>

TABLE 6. COMPARISON OF FEM AND FKP PREDICTIONS.

## 7. CONCLUSIONS

In the present work, a procedure for the development, validation and evaluation of a 3-PRS compliant parallel manipulator has been proposed. To do that, first a study of the solid body kinematics of the mechanism has been performed under the assumption of small displacements, solving both the inverse and forward kinematic problem. The equations of the parasitic displacements as well as the necessary rotations on the revolute and spherical flexure joints are also provided.

Then, a design approach based on FEM analysis for the design of compliant parallel manipulators has been detailed, dividing the mechanical design in two stages, first, the design of the flexure joints, and then, the evaluation of the whole mechanism. The iterative process to achieve the optimal solution for a 3-PRS compliant

mechanism has been shown, providing useful guidelines that relate the overall stiffness, displacement and stresses with the geometrical parameters of the flexure joints.

An experimental validation has been done on a prototype, using an external measurement of both the end platform and the actuated joints position by means of a coordinate measuring machine, verifying first the dimensions of the prototype and then the displacements performed. Those results have been compared with the FKP and FEM estimations during the design stage. The hypothesis of using the solid body kinematics for a compliant mechanism whenever the displacements are small has been experimentally tested, demonstrating that it provides reliable results if the end platform linear displacement is below a 0.9% of the length of the limbs. Above that limit, only FEM calculations must be trusted.

## 8. ACKNOWLEDGMENTS

The authors of this paper wish to acknowledge the financial support received from the Spanish Government via the Ministerio de Educación y Ciencia (Project DPI2011-22955) and Ministerio de Economía y Competitividad (Project DPI2015-64450-R), the ERDF of the European Union, the Government of the Basque Country (Project GIC07/78, IT445-10 and SAIOTEK 2013 SAI13/245, SPC13UN011), and the University of the Basque Country (Project EHUA13/30 and Zabalduz-2012). Thanks are also addressed to Dr. Jorge Presa and Alfonso Urzainki from Egile Corporation XXI for their valuable contributions.

## 9. REFERENCES

- [1] Howell LL. *Compliant Mechanisms*. New York: Wiley; 2001.
- [2] Yue Y, Gao F, Zhao X, Jeffrey Ge Q. Relationship among input-force, payload, stiffness and displacement of a 3-DOF perpendicular parallel micro-manipulator. *Mech Mach Theory* 2010;45:756–71. doi:10.1016/j.mechmachtheory.2009.12.006.
- [3] Merlet J-P. *Parallel Robots*. vol. 208. 2006. doi:10.1007/1-4020-4133-0.
- [4] Wu J, Wang J, Wang L, Li T. Dynamics and control of a planar 3-DOF parallel manipulator with actuation redundancy. *Mech Mach Theory* 2009;44:835–49. doi:10.1016/j.mechmachtheory.2008.04.002.
- [5] Wu J, Chen X, Li T, Wang L. Optimal design of a 2-DOF parallel manipulator with actuation redundancy considering kinematics and natural frequency. *Robot Comput Integr Manuf* 2013;29:80–5. doi:10.1016/j.rcim.2012.07.005.
- [6] Wu J, Li T, Wang J, Wang L. Stiffness and natural frequency of a 3-DOF parallel manipulator with consideration of additional leg candidates. *Rob Auton Syst* 2013;61:868–75. doi:10.1016/j.robot.2013.03.001.
- [7] Kim JJ, Choi YM, Ahn D, Hwang B, Gweon DG, Jeong J. A millimeter-range flexure-based nano-positioning stage using a self-guided displacement amplification mechanism. *Mech Mach Theory* 2012;50:109–20. doi:10.1016/j.mechmachtheory.2011.11.012.
- [8] Shiou F-J, Chen C-J, Chiang C-J, Liou K-J, Liao S-C, Liou H-C. Development of a real-time closed-loop micro-/nano-positioning system embedded with a capacitive sensor. *Meas Sci Technol* 2010;21:054007. doi:10.1088/0957-0233/21/5/054007.
- [9] Yeom T, Simon TW, Zhang M, North MT, Cui T. High frequency, large displacement, and low power consumption piezoelectric translational actuator based on an oval loop shell. *Sensors Actuators A Phys* 2012;176:99–109. doi:10.1016/j.sna.2012.01.001.
- [10] Muraoka M, Sanada S. Displacement amplifier for piezoelectric actuator based on honeycomb link mechanism. *Sensors Actuators A Phys* 2010;157:84–90. doi:10.1016/j.sna.2009.10.024.
- [11] Juuti J, Kordás K, Lonnakko R, Moilanen V-P, Leppävuori S. Mechanically amplified large

- displacement piezoelectric actuators. *Sensors Actuators A Phys* 2005;120:225–31. doi:10.1016/j.sna.2004.11.016.
- [12] Wang W, Han C, Choi H. 2-DOF kinematic XY stage design based on flexure element. 2011 IEEE Int Conf Mechatronics Autom 2011:1412–7. doi:10.1109/ICMA.2011.5985783.
- [13] Yuen Kuan Yong, Aphale SS, Moheimani SOR. Design, Identification, and Control of a Flexure-Based XY Stage for Fast Nanoscale Positioning. *IEEE Trans Nanotechnol* 2009;8:46–54.
- [14] Kim H-Y, Ahn D-H, Chun B-S, Gweon D-G. Development and Optimization of a Novel 3-DOF Precision Flexure Stage. *Proc 10th IEEE Int Conf Nanotechnol Jt Symp with Nano Korea* 2010:903–6.
- [15] Kenton BJ, Leang KK. Design and Control of a Three-Axis Serial-Kinematic High-Bandwidth Nanopositioner. *IEEE/ASME Trans Mechatronics* 2012;17:356–69. doi:10.1109/TMECH.2011.2105499.
- [16] Hao G, Kong X. Design and Modeling of a Large-Range Modular XYZ Compliant Parallel Manipulator Using Identical Spatial Modules. *J Mech Robot* 2012;4:021009. doi:10.1115/1.4006188.
- [17] Yao Q, Dong J, Ferreira PM. A novel parallel-kinematics mechanisms for integrated, multi-axis nanopositioning. *Precis Eng* 2008;32:7–19. doi:10.1016/j.precisioneng.2007.03.001.
- [18] Liang Q, Zhang D, Chi Z, Song Q, Ge Y, Ge Y. Six-DOF micro-manipulator based on compliant parallel mechanism with integrated force sensor. *Robot Comput Integr Manuf* 2011;27:124–34. doi:10.1016/j.rcim.2010.06.018.
- [19] Dunning AG, Tolou N, Herder JL. A compact low-stiffness six degrees of freedom compliant precision stage. *Precis Eng* 2013;37:380–8. doi:10.1016/j.precisioneng.2012.10.007.
- [20] Huijts M, Brouwer D, Dijk J. Design, modeling and control of an elastic parallel kinematic 6-DOFs manipulator. *MiKroniek* 2009;49:420–47.
- [21] Shi H, Su H-J, Dagalakis N. A stiffness model for control and analysis of a MEMS hexapod nanopositioner. *Mech Mach Theory* 2014;80:246–64. doi:10.1016/j.mechmachtheory.2014.05.004.
- [22] Li Y, Xu Q. Kinematic analysis of a 3-PRS parallel manipulator. *Robot Comput Integr Manuf* 2007;23:395–408. doi:10.1016/j.rcim.2006.04.007.
- [23] Bonev IA, Gosselin CM. Geometric analysis of parallel mechanisms. Université Laval, Québec, 2002.
- [24] Nicolae Lobontiu. *Compliant Mechanisms: Design of Flexure Hinges*. Boca Raton, FL: CRC Press; 2002.
- [25] Yong YK, Lu TF. Comparison of circular flexure hinge design equations and the derivation of empirical stiffness formulations. *IEEE/ASME Int Conf Adv Intell Mechatronics, AIM* 2009;32:510–5. doi:10.1109/AIM.2009.5229961.
- [26] Ruiz A, Campa FJ, Roldán C, Altuzarra O. Experimental validation of the kinematics of a 3PRS compliant mechanism for micromilling. *ASME 2015 Int. Des. Eng. Tech. Conf. Comput. Inf. Eng. Conf.*, Boston, Massachusetts, USA: 2015.

## APPENDIX

### A. Forward Kinematics Modeling

Developing Eq. (35) for each leg, the resulting expressions can be obtained:

#### Expressions for Leg 1

$$(OB_1 - OC_1)_x^2 + (OB_1 - OC_1)_y^2 + (OB_1 - OC_1)_z^2 - L^2 = 0 \quad (\text{A.1})$$

The expressions for the components of  $\mathbf{OB}_1$  can be observed in Eq. (6). On the other hand, the vector  $\mathbf{OC}_1$  can be defined as:

$$\mathbf{OC}_1 = \begin{Bmatrix} a - s_1 \\ 0 \\ 0 \end{Bmatrix} \quad (\text{A.2})$$

Therefore, substituting in Eq(A.1), the following equation is reached:

$$(p_x + b \cdot u_x - a + s_1)^2 + (p_y + b \cdot u_y)^2 + (p_z + b \cdot u_z)^2 - L^2 = 0 \quad (\text{A.3})$$

Finally, substituting the expressions of the components of the rotation matrix showed in Eq. (4), the resulting equation for Leg 1 is obtained:

$$(p_x + b(c\theta c\phi + s\psi s\theta s\phi) - a + s_1)^2 + (p_y + bc\psi s\phi)^2 + (p_z + b(-s\theta c\phi + s\psi c\theta s\phi))^2 - L^2 = 0 \quad (\text{A.4})$$

#### Expressions for Leg 2

$$(OB_2 - OC_2)_x^2 + (OB_2 - OC_2)_y^2 + (OB_2 - OC_2)_z^2 - L^2 = 0 \quad (\text{A.5})$$

The expressions for the components of  $\mathbf{OB}_2$  can be observed in Eq. (6). On the other hand, the vector  $\mathbf{OC}_2$  can be defined as:

$$\mathbf{OC}_2 = \begin{Bmatrix} (a - s_2) \cdot \left(-\frac{1}{2}\right) \\ (a - s_2) \cdot \frac{\sqrt{3}}{2} \\ 0 \end{Bmatrix} \quad (\text{A.6})$$

Therefore, substituting in Eq. (A.5), the following equation is reached:

$$\begin{aligned} & \left( p_x - \frac{b}{2} \cdot u_x + \frac{\sqrt{3}b}{2} \cdot v_x + \frac{a - s_2}{2} \right)^2 + \left( p_y - \frac{b}{2} \cdot u_y + \frac{\sqrt{3}b}{2} \cdot v_y - \frac{\sqrt{3}(a - s_2)}{2} \right)^2 + \\ & + \left( p_z - \frac{b}{2} \cdot u_z + \frac{\sqrt{3}b}{2} \cdot v_z \right)^2 - L^2 = 0 \end{aligned} \quad (\text{A.7})$$

Finally, substituting the expressions of the components of the rotation matrix showed in Eq. (4), the resulting equation for Leg 2 is obtained:

$$\begin{aligned}
& \left( p_x - \frac{b}{2}(c\theta c\phi + s\psi s\theta s\phi) + \frac{\sqrt{3}b}{2}(-c\theta s\phi + s\psi s\theta c\phi) + \frac{a-s_2}{2} \right)^2 + \\
& + \left( p_y - \frac{b}{2}(c\psi s\phi) + \frac{\sqrt{3}b}{2}(c\psi c\phi) - \frac{\sqrt{3}(a-s_2)}{2} \right)^2 + \\
& + \left( p_z - \frac{b}{2}(-s\theta c\phi + s\psi c\theta s\phi) + \frac{\sqrt{3}b}{2}(s\theta s\phi + s\psi c\theta c\phi) \right)^2 - L^2 = 0
\end{aligned} \tag{A.8}$$

Expressions for Leg 3

$$(OB_3 - OC_3)_x^2 + (OB_3 - OC_3)_y^2 + (OB_3 - OC_3)_z^2 - L^2 = 0 \tag{A.9}$$

The expressions for the components of  $\mathbf{OB}_3$  can be observed in Eq. (6). On the other hand, the vector  $\mathbf{OC}_3$  can be defined as:

$$\mathbf{OC}_3 = \begin{Bmatrix} (a-s_3) \cdot \left(-\frac{1}{2}\right) \\ (a-s_3) \cdot \left(-\frac{\sqrt{3}}{2}\right) \\ 0 \end{Bmatrix} \tag{A.10}$$

Therefore, substituting in Eq. (A.9), the following equation is reached:

$$\begin{aligned}
& \left( p_x - \frac{b}{2} \cdot u_x - \frac{\sqrt{3}b}{2} \cdot v_x + \frac{a-s_3}{2} \right)^2 + \left( p_y - \frac{b}{2} \cdot u_y - \frac{\sqrt{3}b}{2} \cdot v_y + \frac{\sqrt{3}(a-s_3)}{2} \right)^2 + \\
& + \left( p_z - \frac{b}{2} \cdot u_z - \frac{\sqrt{3}b}{2} \cdot v_z \right)^2 - L^2 = 0
\end{aligned} \tag{A.11}$$

Finally, substituting the expressions of the components of the rotation matrix showed in Eq. (4), the resulting equation for Leg 3 is obtained:

$$\begin{aligned}
& \left( p_x - \frac{b}{2}(c\theta c\phi + s\psi s\theta s\phi) - \frac{\sqrt{3}b}{2}(-c\theta s\phi + s\psi s\theta c\phi) + \frac{a-s_3}{2} \right)^2 + \\
& + \left( p_y - \frac{b}{2}(c\psi s\phi) - \frac{\sqrt{3}b}{2}(c\psi c\phi) + \frac{\sqrt{3}(a-s_3)}{2} \right)^2 + \\
& + \left( p_z - \frac{b}{2}(-s\theta c\phi + s\psi c\theta s\phi) - \frac{\sqrt{3}b}{2}(s\theta s\phi + s\psi c\theta c\phi) \right)^2 - L^2 = 0
\end{aligned} \tag{A.12}$$